Solar methane pyrolysis in a liquid metal bubble column reactor: Effect of medium type and gas injection configuration

Malek Msheik, Sylvain Rodat, Stéphane Abanades

Journal of Analytical and Applied Pyrolysis 183 (2024) 106756

Contents lists available at ScienceDirect

Journal of Analytical and Applied Pyrolysis

journal homepage: www.elsevier.com/locate/jaap

Solar methane pyrolysis in a liquid metal bubble column reactor: Effect of medium type and gas injection configuration

Malek Msheik, Sylvain Rodat, Stéphane Abanades *

CNRS, Processes, Materials and Solar Energy Laboratory (PROMES-CNRS), 7 Rue du Four Solaire, Font Romeu 66120, France

ARTICLE INFO

Keywords:
Turquoise hydrogen
Solar methane pyrolysis
Molten metallic alloys
Molten salts
Gas sparger
Bubble column reactor

ABSTRACT

Solar methane pyrolysis in different molten media and reactor configurations was experimented to improve hydrogen production. Pure Sn, $Ni_{0.18}Sn_{0.82}$, $Cu_{0.45}Bi_{0.55}$, and KCl melts were compared at three different temperatures (1030–1130–1230 °C), and no significant difference was observed except for KCl and only at 1230 °C (X_{CH4} = 72 % vs. 57 % for pure Sn). This enhanced performance was attributed to possible carbon dispersion in the salt, which probably modified the physical properties and enhanced hydrodynamics. A porous quartz sparger (downward injection) did not significantly enhance the bubbles hydrodynamics, mainly because bubbles were trapped and coalesced below the sintered disc. A custom-made sparger (lateral bubbling) did not either improve conversion due to non-uniform pores. A sparger with an upward injection should be preferred to generate small bubbles with longer residence time. When a solid bed of tungsten carbide particles was placed around the injector, overlaid by molten tin, the conversion was improved even at a relatively low temperature (X_{CH4} = 17 % at 1030 °C). The immersed bed likely behaved as a porous device and increased the gas-solid surface contact. Combining particle bed and liquid bubbling system is very promising for further optimization of methane pyrolysis in molten media. The carbon collected above molten metals showed mostly a sheet-like structure with significant metal contamination. In case of KCl, most carbon was entrained with the gas, while the remaining was mixed with KCl in the reactor. The density of KCl is close to that of carbon, which prevented a good separation.

1. Introduction

Hydrogen production worldwide in 2022 resulted in 12–13.5 kg-CO_2/kg-H_2 because H_2 was mainly produced from fossil fuels through CO_2-emitting processes such as Steam Methane Reforming (SMR) and Coal Gasification (CG). According to the International Energy Agency (IEA), more than 78 % of hydrogen demand in 2020 (90 Mt) was produced through SMR and CG owed to their cheapest production costs [1–3] (Figure S1). Carbon Capture, Utilization and Storage (CCUS) for low-carbon H_2 increases the cost of H_2 production and is still inefficient enough for long term storage. Green hydrogen produced through water dissociation (electrolysis) is net zero carbon, yet the production cost is very high (3.7 €/kg H_2 for water electrolysis using wind energy against 1.07–1.87 €/kg H_2 and 0.62–1.42 €/kg H_2 for SMR with and without CO_2 sequestration, respectively) [4].

Alternatively, H_2 can be produced through the endothermic methane cracking reaction (Eq. 1) [5–7]. Methane pyrolysis refers to turquoise H_2 as it may be a transitional technology between SMR with CCUS (blue H_2) and water electrolysis (green H_2) [5,8]. Solar methane cracking benefits from concentrated solar energy (CSE) as the heating source to produce hydrogen and solid carbon without CO/CO_2 emissions from the reaction [9–12].

$$CH_{4(g)} \rightarrow 2H_{2(g)} + C_{(s)} \qquad \Delta H^{\circ} = 74.85\ \text{kJ}\Big/\text{mol of } CH_4 \tag{1}$$

Conventionally, methane was dissociated in gas-phase reactors possibly containing solid catalysts [10,13–16]. Here, common issues were catalyst coking and reactor clogging under severe operating conditions due to carbon deposition on the hot walls [17]. Pyrolysis in molten media garnered more attention in the last few years, although this path dates back to 1931 [18]. In bubble columns, methane is injected through hot liquid metals or salts and hence, heat and mass transfer are improved under suitable gas-liquid hydrodynamics [19,20]. The high temperature allows splitting methane into hydrogen gas leaving with the outlet stream and solid carbon, which floats atop the liquid driven by density difference [21,22]. In short, methane cracking for hydrogen production might offer a midterm solution for a sustainable H_2 production [5].

* Corresponding author.
E-mail address: stephane.abanades@promes.cnrs.fr (S. Abanades).

https://doi.org/10.1016/j.jaap.2024.106756
Received 18 May 2024; Received in revised form 19 August 2024; Accepted 9 September 2024
Available online 11 September 2024

The main studies of methane cracking in molten media in literature focus on two different aspects: the molten medium and the type of the gas injector. Concerning the type of the melt, $Ni_{0.27}Bi_{0.73}$ [23], $Cu_{0.45}Bi_{0.55}$ [24], Mg [25], and Te [26] were reported as suitable liquid media for methane cracking. Others investigated Sn [27–31] and Bi [32], and reported inert or low catalytic performance. Bimetallic NiSn alloy was also investigated by Sorcar and Rosen [33] who found that it reduced the activation energy of the pyrolysis reaction. Several salts were also investigated like KCl, NaCl, KBr, NaBr [34–36], $MnCl_2$/KCl [36,37], $MnCl_2$/KBr [38], and metal sulfides (MoS_2) suspended in molten NaBr/KBr salt [39]. $MnCl_2$/KCl was the best salt mixture in terms of catalytic activity, where the performance was better than either pure KCl or $MnCl_2$, due to the lower activation energy of the mixture (161 kJ/mol). Rahimi et al. [40] were the only to conduct methane cracking in a two-phase bubble column, where Ni-Bi molten metal alloy was overlaid by KCl or NaBr molten salt. This study chiefly proved the production of a purer carbon byproduct since metals were condensed in the salt phase.

Other studies focused on the gas injector to increase methane conversion in the bubble column by improving hydrodynamics of bubbles. Leal Pérez et al. [41] used a 0.2 mm gas sparger in molten gallium, which allowed them to reach 91 % methane conversion at a relatively low temperature (1119 °C). The effect of the gas injector in molten $Ni_{0.34}Sn_{0.66}$ was also studied by Kim et al. [42] with a homemade ceramic sparger made of zirconia balls fixed around the outlet of the injector using zirconia paste. The sparger decreased the bubbles diameter from 3–8 mm (when using a normal open-end injector) to 0.5 mm, and hence boosted methane conversion from 15 % to 97 %. Even molten tin was tested with the use of a 0.5 μm gas sparger, which led to 51 % methane conversion at only 750 °C [29]. These results highlighted the definite effect of the gas injector on the hydrodynamics of bubbles and consequently on methane conversion.

A challenge of molten-media methane pyrolysis is the continuous separation of carbon. Von Wald et al. [43] stated that the accumulated carbon could be removed by entrainment in the effluent gas. Kudinov et al. [44] proposed to insert a floating structure in the reactor to detect the level of the surface. When the level rises above a given threshold, the accumulated carbon has to be removed through vacuum. Other challenges are related to improving the hydrodynamics of bubbles [45,46], e.g. via a suitable design of the gas sparger to boost methane conversion [47,48]. More research is also required to reduce contamination of the floating solid carbon by entrained metal or salt [40,49]. The carbon properties are also very important for the process scale-up since a premium carbon quality will improve the economics of the process and make it competitive with SMR which is still the cheapest process for H_2 production [50]. Hydrogen production cost via methane cracking is in the range 2–3.56 €/kg depending on the technology [51,52]. Rodat et al. [53] showed that the H_2 production cost decreases when the added value of carbon increases. In a molten metal system, selling the carbon product significantly reduces the H_2 cost and makes it competitive with SMR when a tax of 50 €/t CO_2 is imposed [41].

To date, there is no reported experiment on molten-media methane pyrolysis in solar reactors, while electric furnaces were used instead. Solar reactors were only implemented for gas-phase methane pyrolysis, as detailed previously in a review [6]. In another work, uncatalyzed pyrolysis in gas phase was demonstrated to be more efficient than pyrolysis in molten tin mostly because of a higher residence time in gas phase [54]. In this work, solar experiments for optimization of the methane pyrolysis process were elaborated. These experiments were meant to improve methane conversion in liquid phase and the considered strategies could be split into two main categories:

- The first set of experiments focused on screening the effect of the molten medium on methane conversion, whether through the intrinsic catalytic activity of the melt or its physical properties that may affect hydrodynamics of bubbles. Different molten media (metal alloys and salt) with the presence of catalytic species (e.g., Ni) were considered to elucidate whether or not they can exhibit a significant effect. Several melts such as pure Sn, $Ni_{0.18}Sn_{0.82}$ (10:90 wt%), and $Cu_{0.45}Bi_{0.55}$ (20:80 wt%) alloys, as well as KCl salt were compared to study their influence on methane pyrolysis performance. Such a direct comparison was never proposed previously.
- The second set of experiments was carried out with pure molten Sn, while using different injectors (quartz sparger, custom-made sparger) or different configurations (bed of solid particles settled around the orifice). The type of sparger or gas disperser was studied as it may influence the size and rising time of bubbles, and thereby the methane conversion. The aim was to find the best injection design that efficiently improves hydrodynamics.

The main performance metrics including gas product composition, methane conversion, hydrogen and carbon yields, and carbon product characteristics were thoroughly assessed, and the main influencing factors affecting methane pyrolysis were also discussed. An innovative configuration including an immersed packed bed of tungsten carbide in liquid tin was proposed and assessed. This study considers for the first time various configurations for methane conversion improvement, and further demonstrates the potential of solar-driven methane pyrolysis in molten media as a promising route toward clean production of hydrogen and solid carbon.

2. Experimental set-up and methods

2.1. Solar reactor description

A solar tubular reactor for methane pyrolysis was designed and installed at PROMES-CNRS laboratory in France (Fig. 1). In the section of each set of experiments, the relevant configuration variants will be detailed (Figures S2(a) and S3 in the supporting information). Generally, the reactor consisted of two coaxial tubes made of alumina (Al_2O_3) where the reaction took place. Ceramic reactor materials were used for the tube and injector to withstand both high temperatures and corrosiveness of molten media. As alumina is opaque, the concentrated solar flux was used only to heat the reactor up to the desired operating temperature, so that no photochemistry was involved. These tubes were centered in a cylindrical insulation layer to reduce heat losses. The insulation was 70 mm thick, made of alumino-silicate fibers (UltraBoard 1600/400). Inner and outer tubes had lengths of 500 mm and 315 mm, inner diameters of 3 mm and 23 mm, and outer diameters of 6 mm and 30 mm, respectively. The outlet of the inner tube was held 10 mm above the bottom of the outer one. The reactor was heated through a 50 mm high solar cavity receiver with a 15 mm diameter aperture. The cavity absorbed the concentrated solar flux received from a 1.5 kW (thermal) heliostat-parabola solar system (2 m diameter parabolic dish with a peak concentration ratio of about 15000 and focal distance of 0.85 m). Further description of the solar heating system can be found in previous studies [6,54]. The molten medium was thus indirectly heated by solar energy via an intermediate heat transfer tube. Ar and CH_4 were injected via the central inner tube and then flowed through the molten bath (flow-rates controlled by two mass-flow controllers). Two pressure sensors measured the inlet and outlet pressures (P_1/P_2). At the outlet, two microfilters in series separated the transported carbon particles and the gas then flowed through a water bubbler for gas cleaning. Finally, the gas composition was continuously measured by an online gas analyzer (Emerson NGA2000) equipped with TCD and NDIR sensors for H_2 and CH_4, respectively. In addition, a micro-GC (Varian CP4900) measured the species mole fractions every 2–3 minutes (H_2, CH_4, and C_2H_y).

2.2. Materials and methods

Methane (purity > 99.95 %) and argon (purity > 99.999 %) were

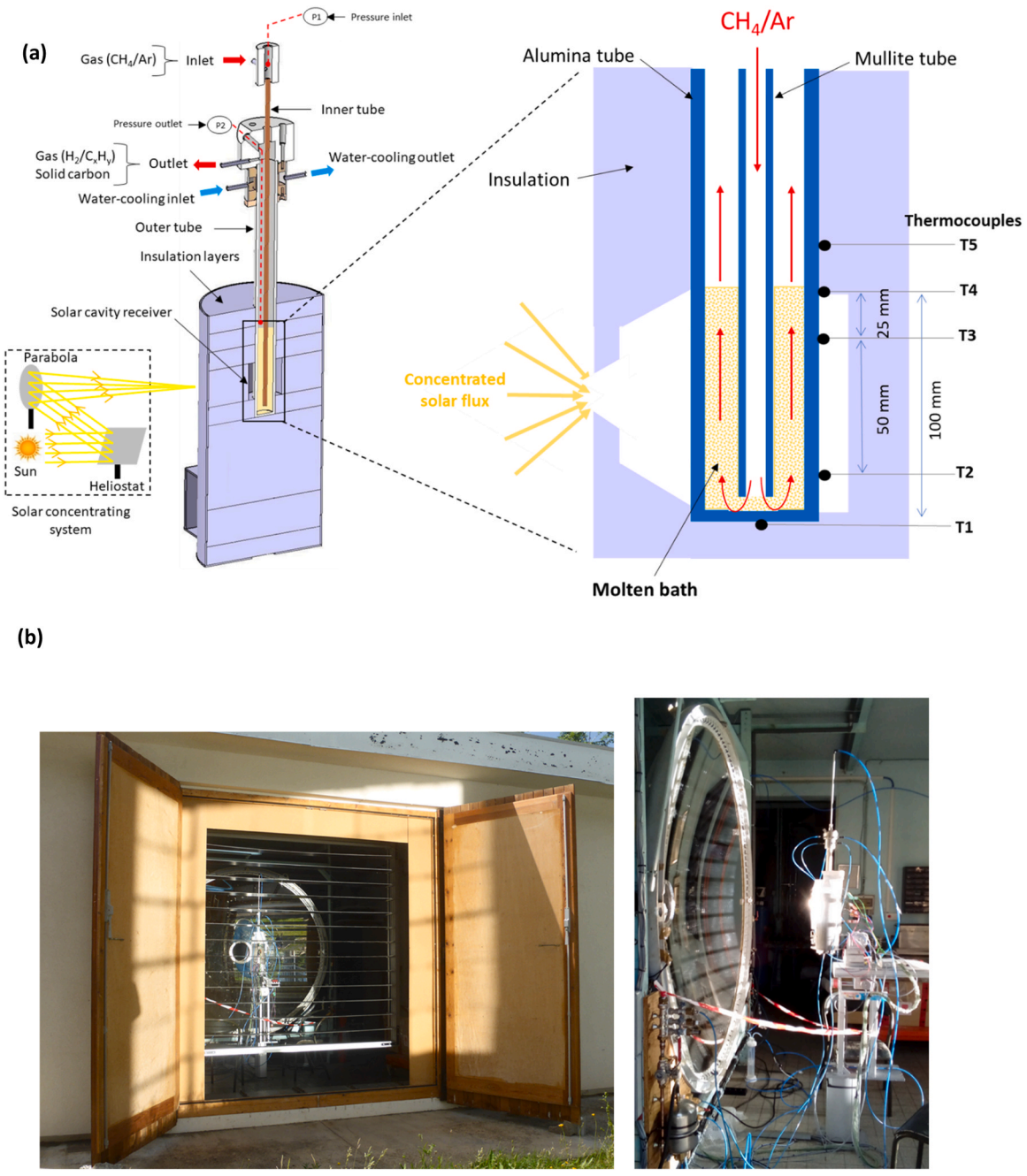

Fig. 1. Solar bubble column reactor for methane pyrolysis in molten media: (a) cross-section scheme, (b) photographs of the reactor at the focus of a 2 m diameter solar concentrator.

supplied from Air Liquide (France). Metal powders and potassium chloride were purchased from Fisher Scientific (France) with the following purities and sizes: Sn (99.5 %, -100 mesh), Ni (99+%, -100 mesh), Cu (99 %, -325 mesh), Bi (99.5 %, -100 mesh), and KCl (99 %).

Methane conversion (X_{CH4}), hydrogen yield (Y_{H2}), and carbon yield (Y_C) were calculated through Eqs. (2), (3), and (4), respectively [54,55]:

$$X_{CH_4} = 1 - \frac{y_{CH_4}.F_t}{F_{0,CH4}} \quad (2)$$

$$Y_{H_2} = \frac{y_{H_2}.F_t}{2F_{0,CH_4}} \quad (3)$$

$$Y_C = 1 - \frac{\sum x.y_{C_xH_y}.F_t}{F_{0,CH_4}} \quad (4)$$

where y_i are species mole fractions in the outlet stream. The following hydrocarbons were considered: CH_4, C_2H_2, C_2H_4, and C_2H_6. $F_{0,CH4}$ is the inlet molar flow rate of methane (mol/min). The method for uncertainties calculation is detailed in Supporting Information.

The total outlet molar flow rate (F_t) was calculated as follows:

$$F_t = \frac{F_{Ar}}{1 - y_{H_2} - \sum y_{C_xH_y}} \quad (5)$$

where F_{Ar} is the outlet molar flow rate of argon which is equal to its inlet flow rate $F_{0,Ar}$ (mol/min) because argon is inert.

According to Tate's law, which is used to estimate bubbles diameter in a single bubbling regime (no coalescence), the physical properties of the liquid medium may affect the bubble diameter. Thus, Tate's law

shown in Eq. (6) was used to compare the ratio of bubbles diameter in different melts.

$$D_b = \left(\frac{12\, R_0 \,.\sigma}{(\rho_l - \rho_g).g} \right)^{\frac{1}{3}} \quad (6)$$

where R_0 is the feeder inner radius (m), σ (N/m) and ρ_l (kg/m^3) are the surface tension and the density of the melt, and ρ_g is the gas density (kg/m^3), which could be neglected compared to ρ_l.

The void fraction ε of a solid bed immersed in the liquid bath (equivalent to the volume of fluid filling the void) is important to adjust the total melt height, whenever a solid bed is set around the orifice to enhance hydrodynamics. It can be calculated as follows:

$$\varepsilon = 1 - \frac{\rho_{apparent}}{\rho_{absolute}} \quad (7)$$

Where $\rho_{apparent}$ (kg/m^3) is the apparent density of the bed while $\rho_{absolute}$ (kg/m^3) is the true density of the solid material constituting the bed.

2.3. Medium type

2.3.1. Molten metals vs. molten salts

Several experiments in different liquid media were conducted with an expected catalytic effect to improve methane conversion (Table 1). The melt height was fixed to 100 mm, as illustrated in Figure S2. Five thermocouples were implemented (T1-T2-T3-T4: type S; T5: type K) and the operating temperature in the melt was controlled based on the average of T2 and T3, corresponding to the thermocouples that are in symmetrical positions (top and bottom) in the solar cavity. The configuration shown in Figure S2(a) corresponds to the set of experiments with different liquid media (Sn, $Ni_{0.18}Sn_{0.82}$ (10:90 wt%), $Cu_{0.45}Bi_{0.55}$ (20:80 wt%), and KCl).

The first medium was pure molten tin used as a reference case. 259 g of Sn were weighed to form a melt height of 100 mm in the tubular reactor. The gas inlet flow rate Q_0 was fixed at 0.25 NL/min with an inlet methane molar fraction $y_{0,CH4}$ of 0.3. Three consecutive runs were conducted at three different temperatures (1030–1130–1230°C). These operating conditions were applied to all the experiments whatever the melt used (Table 1).

Nickel is one of the best metallic catalysts for methane cracking in gas phase, resulting in a very low activation energy (65 kJ/mol) [56]. Thus, a molten metallic alloy of nickel and tin was investigated as a second medium. 26 g of Ni and 238 g of Sn (10:90 wt% or 18:82 mol%) were weighed and mixed together in their powder state. According to Ni-Sn phase diagram, this alloy melts at around 750 °C [57]. Adding more nickel to the mixture would increase the melting temperature making processing more complex.

In literature, the metallic alloy with the best reported catalytic activity was $Cu_{0.45}Bi_{0.55}$ [24], which outperformed $Ni_{0.27}Bi_{0.73}$ [24]. Cu was not reported as a better catalyst than Ni [6], but it is probable that the Cu-Bi metal alloy formed a bulk with favorable physical properties for methane pyrolysis. Thus, a third alloy was investigated by blending 70 g Cu and 283 g Bi (20:80 wt% or 45:55 mol%) to form a melt of 100 mm height at 1000 °C.

There is no experimental study comparing directly methane conversion in a molten metal and in a molten salt. Therefore, potassium chloride salt (KCl) was investigated in the same configuration (Figure S2) and under the same operating conditions for direct comparison with molten metals (KCl melting point: 770°C, boiling point: 1420°C). The maximum temperature of 1230°C was used to warrant that no significant vaporization occurs during the experiments. KCl was used due to its cheapness and thermal stability, but other salts such as $MnCl_2$/KCl and $FeCl_3$/KCl could be used in future works to compare their catalytic activity.

2.3.2. Bed of solid alumina particles

Instead of molten media, a bed of solid alumina particles was also investigated in order to assess to which extent an inert solid bed may improve heat and mass transfer and hence methane conversion in a solar tubular reactor. These experiments aimed to show the beneficial effect of the inert particles bed and the catalytic activity of Ni as solid particles (for a comparison with Ni dissolved in molten bath).

Alumina particles (diameter in the range 0.2–0.4 mm) were used to create a solid bed of 100 mm height in the reactor. This bed thus substituted molten media. The required weight of alumina was calculated. Based on the true density of alumina (3.96 g/cm^3) and apparent density of the alumina bed (0.91 g/cm^3), the calculated void fraction (Eq. 7) was 77 %. Thus, 35.5 g of Al_2O_3 particles were weighed (equivalent to 100 mm height) and inserted in the reactor (Figure S2).

Two solar pyrolysis experiments in solid-bed were carried out, one with only alumina particles inside the reactor and the other with the addition of 26 g of solid Ni powder to assess solid Ni catalytic effect (Ni/Al_2O_3: 56:44 mol% or 42:58 wt%). The use of Ni catalyst was considered to show the difference between the catalytic activity of Ni in solid state vs. Ni in molten NiSn alloy. The presence of Ni could occupy 7 mm theoretically (ρ_{Ni} = 8.29 g/cm^3 at 1000 °C). However, given the difference in particle size, this amount of Ni filled the void fraction between alumina particles, which did not affect the total height of the bed (100 mm). For each experiment, the operating conditions were similar to those of the experiments with molten media (Q_0 = 0.25 NL/min with $y_{0,CH4}$ = 0.3).

2.4. Gas injection configurations

The previous section introduced the different selected media in the first set of experiments. This section presents the second set, through three innovative injection configurations.

2.4.1. Quartz sparger

A quartz sparger was used to investigate its effect on methane cracking in molten tin (Figure S4). The sparger was made of a long tube

Table 1
Results of methane cracking experiments with different molten media (Q_0 = 0.25 NL/min and $y_{0,CH4}$ = 0.3).

Medium	T (°C)	y_{H2}	y_{CH4}	y_{C2H2} (ppm)	y_{C2H4} (ppm)	y_{C2H6} (ppm)	X_{CH4} (%)	Y_{H2} (%)	Y_C (%)
Sn	1030	0.003	0.296	15	509	530	1	1	1
Sn	1130	0.078	0.228	4840	5096	601	22	13	15
Sn	1230	0.256	0.114	7142	2933	125	57	48	49
$Ni_{0.18}Sn_{0.82}$	1030	0.003	0.292	3	864	486	3	1	2
$Ni_{0.18}Sn_{0.82}$	1130	0.030	0.256	1699	3990	849	15	5	11
$Ni_{0.18}Sn_{0.82}$	1230	0.254	0.124	7057	3685	202	53	48	44
$Cu_{0.45}Bi_{0.55}$	1030	0.002	0.295	7	2202	1383	2	0	0
$Cu_{0.45}Bi_{0.55}$	1130	0.061	0.229	3939	6550	780	23	10	16
$Cu_{0.45}Bi_{0.55}$	1230	0.252	0.120	10958	5380	208	54	48	42
KCl	1030	0.000	0.300	0	0	0	0	0	0
KCl	1130	0.113	0.223	1222	3054	344	21	20	18
KCl	1230	0.347	0.069	7403	3580	134	72	71	63

(inner and outer diameters: 3 and 6 mm, length: 690 mm) with a porous orifice (sintered quartz disc with pores size ranging from 40 to 100 μm). The sparger was immersed in a 100 mm bath of molten tin (Figure S2). The only difference of this configuration in Figure S2 was thus the inner tube that was substituted by the quartz sparger in order to create small bubbles.

2.4.2. Custom-made sparger

A porous ceramic sparger, made from the same material as the insulation around the reactor tube (polycrystalline mullite/alumina wool, PCW), was shaped (20 mm height and 15 mm diameter cylinder). The porous customized sparger is referenced as PCW sparger and it is shown in Figure S5. This custom-made sparger provides sideways bubbling (lateral bubbling), which makes a fundamental difference compared to the quartz sparger bubbling downwards.

To fabricate it, a porous cylinder was pierced from the top for insertion of a 1 m mullite tube (until the tube can reach the central height). The mullite tube was inserted in the hole and the connection was sealed with cement (Resbond 903HP). The cement was heated with an electric heater (Kanthal MS31) for almost 4 h at 380 °C to guarantee its robustness. This sparger was tested in a 150 mm-height bath of molten tin with the configuration shown in Figure S3(a) (tin melt height was increased to 150 mm compared to 100 mm in previous experiments to increase the length below the heated cavity and avoid carbon formation in the sparger). This experiment was part of a set of three experiments (Figure S3): (1) with PCW sparger, (2) with an open-end tube (to compare results of the first with a simple injection design), and (3) with a bed of tungsten carbide (WC) particles (as detailed in the next subsection).

2.4.3. Tungsten carbide (WC) bed

The concept of solid particle bed immersed in liquid metal was finally proposed. Combining the beneficial effects of particle bed immersed in a molten bath was investigated to promote methane conversion. Moreover, the combination of both molten metal and particle bed should improve bubble residence time.

To prepare the WC bed, non-uniform particles of tungsten carbide (WC) (0.2–0.3 mm size) were filled in the reactor to make a solid bed around the orifice of an open-end tube. More details about the way they were inserted in the reactor can be found in supporting information. Tungsten carbide particles have an apparent density of 10 g/cm^3 and an absolute (true) density of 15.8 g/cm^3 ($\varepsilon = 37$ % based on Eq. (7)). Such a density is much higher than that of molten tin (6.5 g/cm^3), which should make WC particles settle down around the orifice of the injector and ensure their immersion in the liquid. Moreover, WC has a very high melting point (2870 °C), which prevents the particles to melt and to form an alloy with liquid tin [58]. WC is also highly resistant to corrosion [59].

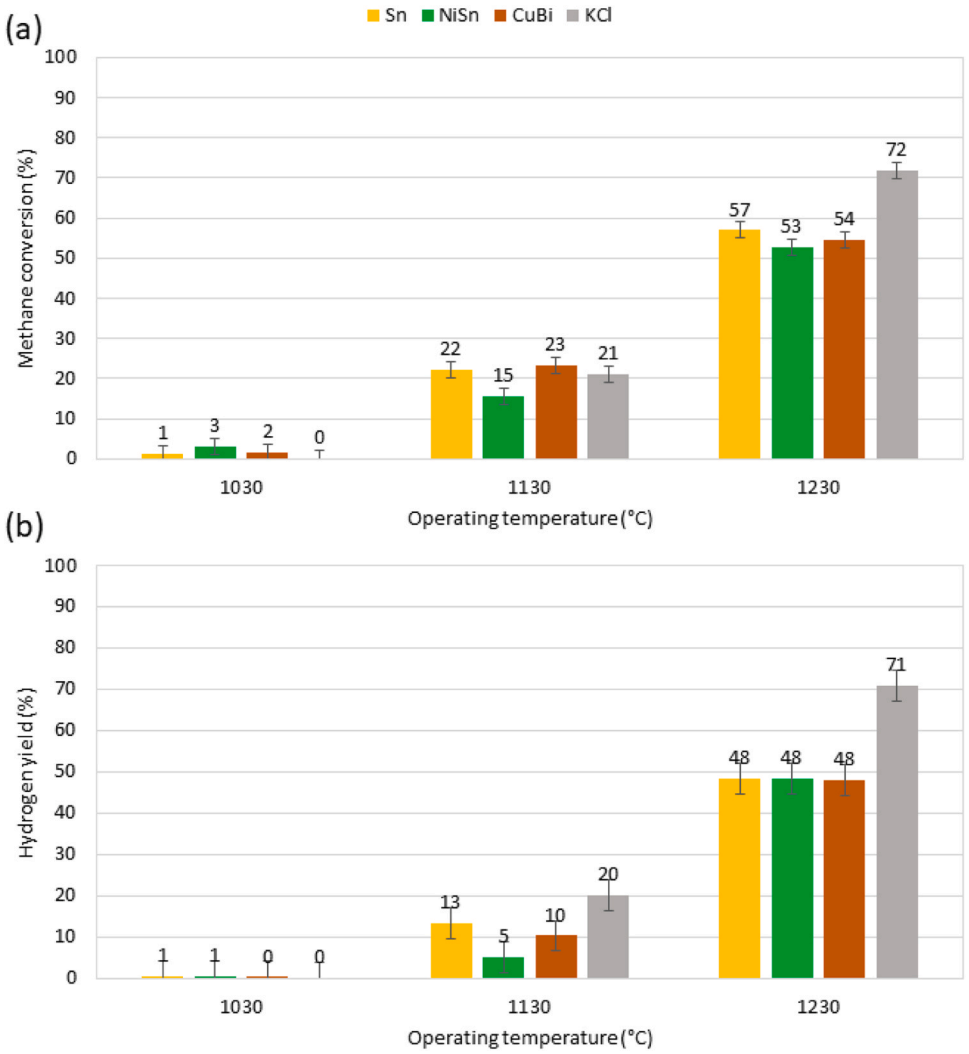

Fig. 2. Methane pyrolysis performance as a function of temperature in different melts: (a) methane conversion, (b) hydrogen yield.

3. Results and discussion

3.1. Influence of the medium type

3.1.1. Molten metals vs. molten salts

This section aimed to compare molten bimetallic alloys (CuBi, NiSn) and molten KCl with pure liquid Sn, in the same reactor configuration and operating conditions, to show whether a catalytic activity can be evidenced or not. The results of the experiments in a 100 mm-height bath of different media are summarized in Table 1.

For a better results visualization, a bar graph of methane conversion and hydrogen yield is shown in Fig. 2. At 1030 °C, there was almost no methane decomposition regardless of the melt type in the reactor. This temperature was too low for significant methane conversion in a bubble column solar reactor with the current gas flow rate (0.25 NL/min). A much lower flow rate can significantly enhance methane conversion. A detailed study about the effect of residence time and other operating conditions on methane conversion was presented in previous studies [54,55]. Note that the residence time in the case of bubbling reactor corresponds to the formation and rising time of bubbles.

When the temperature was increased to 1130 °C, methane conversion in pure Sn reached 22 % with 13 % hydrogen yield. Methane conversions with $Cu_{0.45}Bi_{0.55}$ and KCl were very close (X_{CH4} = 23 % vs. 21 % and Y_{H2} = 10 % vs. 20 %, respectively). The difference in hydrogen yield was directly related to the hydrogen molar fraction in the outlet gas, which was significantly higher in KCl (0.113) than in $Cu_{0.45}Bi_{0.55}$ (0.061). Surprisingly, the conversion in $Ni_{0.18}Sn_{0.82}$ was the lowest with only X_{CH4} = 15 % and Y_{H2} = 5 %. Although this was not a high difference compared to Sn, $Cu_{0.45}Bi_{0.55}$ and KCl when considering the uncertainties (calculation method given in Supporting Information), a nickel-containing alloy was supposed to improve methane conversion beyond pure Sn at least. This result contradicts previous studies about enhanced catalytic effect in Ni-containing alloys [23,27].

At 1230 °C, methane conversion in pure Sn increased to 57 % with 48 % hydrogen yield. Similarly, X_{CH4} and Y_{H2} in $Cu_{0.45}Bi_{0.55}$ and $Ni_{0.18}Sn_{0.82}$ were very close to pure Sn (X_{CH4} = 54 % vs. 53 % and Y_{H2} = 48 % vs. 48 % for $Cu_{0.45}Bi_{0.55}$ and $Ni_{0.18}Sn_{0.82}$, respectively). In all these experiments, methane conversion increased with increasing temperature because the reaction is endothermic. Unlike the first two temperatures (1030 °C and 1130 °C), methane conversion in KCl at 1230 °C significantly surpassed all molten metals with X_{CH4} = 72 %. The absolute difference was 15 % with pure molten Sn (X_{CH4} = 57 %) and was completely out of the uncertainty range.

The fact that KCl performance was boosted only at the highest temperature (1230 °C) did not support the hypothesis of a better catalytic activity of KCl compared to molten Sn, $Ni_{0.18}Sn_{0.82}$ and $Cu_{0.45}Bi_{0.55}$. Using Eq. (6) to estimate the bubbles diameter formed in molten Sn (D_{b_Sn}) vs. KCl (D_{b_KCl}) at 1230 °C, the calculated diameter ratio was then 1.11, based on Eq. (8) (melt properties at 1230 °C were found in references [60,61]).

$$\frac{D_{b_{Sn}}}{D_{b_{KCl}}} = \left(\frac{\sigma_{Sn}}{\rho_{Sn}} \times \frac{\rho_{KCl}}{\sigma_{KCl}}\right)^{\frac{1}{3}} = \left(\frac{0.482}{6390} \times \frac{1260}{0.069}\right)^{\frac{1}{3}} = 1.11 \quad (8)$$

Hence, the difference in the size of bubbles was relatively small, which could not completely explain the superior performance of KCl at 1230 °C. A more reasonable explanation may be directly related to carbon byproduct formed during methane decomposition. In fact, carbon density generally varies between 0.95 and 3 g/cm^3 depending on its crystallinity. Carbon produced in molten media is more likely graphitic whose density is about 2 g/cm^3. KCl density is 1.26 g/cm^3 at 1230 °C, a significantly smaller difference with carbon density compared to metal densities usually above 6 g/cm^3 [6]. This issue could prevent carbon from floating on the surface of KCl and left it dispersed inside the molten salt phase. Some carbon was thus accumulated in the melt during the successive runs from 1030 °C to 1230 °C (this phenomenon has been noticed after the experiments and a clear difference in carbon flotation was evidenced and presented in Figure S6). Carbon dispersion in the salt made the bulk more viscous while carbon was formed from the pyrolysis reaction. Changing the physical properties of the bulk can modify hydrodynamics toward favorable conditions, especially related to the increase of the residence time of bubbles. For instance, if carbon increased the viscosity of KCl, the bubbles would have slowed down while rising due to the increased viscosity. This hypothesis related to the changed physical properties of KCl at 1230 °C during reaction was supported by the fact that the better performance of the salt only appeared at this highest temperature after some carbon had formed and dispersed in molten KCl.

In summary, bimetallic alloys such as $Ni_{0.18}Sn_{0.82}$ and $Cu_{0.45}Bi_{0.55}$ did not improve methane conversion compared to pure Sn. The activities of the different liquid media are compared at a given residence time (i.e., same gas flow rate and bath height). Thus, it can be clearly observed that the activity does not change at given operating conditions. This suggests that liquid-phase catalysts have no significant effect on the methane pyrolysis performance. These results contradict reported studies in literature about the catalytic effect of $Cu_{0.45}Bi_{0.55}$ [24] and $Ni_{0.18}Sn_{0.82}$ [27]. A catalytic activity was assigned to these media in literature, although the better performance may also be attributed to the different operating conditions. For instance, Zaghloul et al. [27] used a similar height of molten media (100 mm) but only injected 0.07 NL/min of gas in the melt (vs. 0.25 NL/min in this study). The flow rate and bubbles size/residence time have a strong impact and have to be considered when comparing conversion results from various studies. Regarding KCl, Kang et al. [36] obtained 30 % methane conversion in molten KCl:$MnCl_2$ at 1050 °C and such a result could also be attributed to the much lower gas inlet flow rate (0.02 NL/min in [36]), along with a catalytic effect of KCl:$MnCl_2$ mixtures. However, the authors also mentioned the increasing carbon suspended in the melt, which might increase the bubble residence time and be ultimately the reason for the enhanced conversion. KCl did not appear to be a better catalytic medium compared to pure Sn, especially at 1030 °C and 1130 °C. However, the higher density of solid carbon as compared to that of KCl probably led to carbon dispersion in KCl, thereby changing the physical properties of the molten medium. Such conditions may lead to favorable bubbles hydrodynamics (increase of the bubbles residence time) and improved conversion, but are not suitable for a continuous carbon recovery in the process. As carbon separation is the main advantage expected from molten media pyrolysis, the fact that carbon remains mixed with the salt is a strong limitation (in addition to corrosive and volatile issues), and therefore molten metals are more suitable than salts.

SEM/EDX and XRD analyses of $Ni_{0.18}Sn_{0.82}$, $Cu_{0.45}Bi_{0.55}$, and KCl solidified pellets extracted after the experiments were carried out and presented in the supporting information (Figs. S7-S15). These analyses allowed to determine the chemical composition of the solidified metallic alloys ($Ni_{0.18}Sn_{0.82}$ and $Cu_{0.45}Bi_{0.55}$) and KCl after reaction. They further confirmed the absence of metals segregation along the liquid bath height (along the axial direction). Both metals were thus well distributed in the whole melt despite density difference. The large amount of carbon (> 16 wt%) dispersed in KCl was also evidenced. The carbon samples recovered after these experiments were also analyzed separately and data are reported in the supporting information (Figs. S16-S25). Briefly, in the case of metal alloys ($Ni_{0.18}Sn_{0.82}$ and $Cu_{0.45}Bi_{0.55}$), all the carbon was collected at the surface of the liquid and showed mainly a sheet-like graphitic structure, while containing metal particles (especially Sn or Bi) due to metal entrainment with rising bubbles. In the case of KCl, carbon remained dispersed in the salt while a significant part was also recovered in the filter in the form of spherical particles contaminated with KCl due to the high salt volatility. This suggests that fine condensed salt droplets can be entrained by the carrier gas along with solid carbon.

3.1.2. Performance with an alumina bed

Runs with alumina bed were carried out for hours to check the

stability of the process. Outlet mole fractions of H_2 and CH_4, as well as temperature and pressures at the reactor inlet and outlet (P1 and P2) are represented as a function of the operating time in Fig. 3. For each experiment (with or without Ni), three different bed temperatures were studied (1000–1100–1200 °C). Pressures were stable at 900 mbar in both experiments. Process stability was demonstrated for over 6 hours of continuous operation. The averaged results of methane cracking with a bed of solid alumina particles at each temperature are summarized in Table 2. Methane conversion and hydrogen yield were both represented in Fig. 4. As a result, the bed had a very important role in increasing methane conversion, as compared to molten media, in both experiments even at low temperatures. X_{CH4}, Y_{H2}, and Y_C were 38 %, 37 %, and 38 %, respectively at 1000 °C in the experiment with only alumina bed inside. In molten media, the conversion was negligible at a similar temperature (1030 °C) and was still lower even at 1130 °C (X_{CH4} = 23 % for $Cu_{0.45}Bi_{0.55}$). This drastic increase in methane conversion was clearly attributed to the high gas-alumina interface, which boosted heat transfer as well as methane decomposition at the solid surface.

In the second experiment with Ni contained in the alumina bed, the performance was far more improved at 1000 °C (X_{CH4} = 73 %, Y_{H2} = 72 %, and Y_C = 72 %). The presence of Ni thus boosted methane decomposition thanks to its high catalytic activity. Methane conversion was enhanced as temperature increased until it reached 93 % and 94 % at 1200 °C for the experiment without and with Ni, respectively. The catalytic activity of Ni was more pronounced at lower temperatures (1000 and 1100 °C) where the difference in methane conversion between experiments with and without Ni was higher. At 1200°C, the reaction conversion is almost complete due to the absence of kinetic limitation and the catalyst effect is thus not observable. As the temperature increased, favorable thermodynamics improved the conversion whether or not the catalyst was present. The improved conversion at low temperatures due to the catalytic activity of Ni was thus highlighted. This also means that the catalytic activity of Ni in solid phase was effective, whereas no significant effect was noticed with liquid phase catalysts (case of NiSn or CuBi molten mixtures).

During these two experiments in a solid bed of alumina particles, negligible molar fractions of secondary hydrocarbons in the outlet gas were noticed (Table 2) compared to experiments in molten media (Table 1). For instance, C_2H_2, C_2H_4, and C_2H_6 were almost not found in the outlet gas in the experiment with Ni in the bed. Similarly, molar fractions of C_2H_2, C_2H_4, and C_2H_6 were also negligible in the case of the pure alumina bed (e.g., 41 ppm, 42 ppm, and 81 ppm for C_2H_2, C_2H_4, and C_2H_6 at 1200 °C, respectively). The low presence of secondary hydrocarbons resulted in a hydrogen yield very close to methane conversion in these two experiments (Fig. 4).

The main drawback of such a configuration is the deposition of carbon on the particle surface and thus the difficult separation, which makes continuous operation with the same particle bed practically impossible. It should be noted that immersing alumina particles in molten metal to favor carbon separation is not possible due to the low density of alumina. The carbon samples recovered after experiments (mixed with alumina bed) were analyzed separately (results are reported in a dedicated section for carbon analysis in SI, Figs. S26-S27). Carbon spread on the surface of alumina particles and was also spherical and graphitic with more chains of spheres when there was presence of nickel powder in the bed.

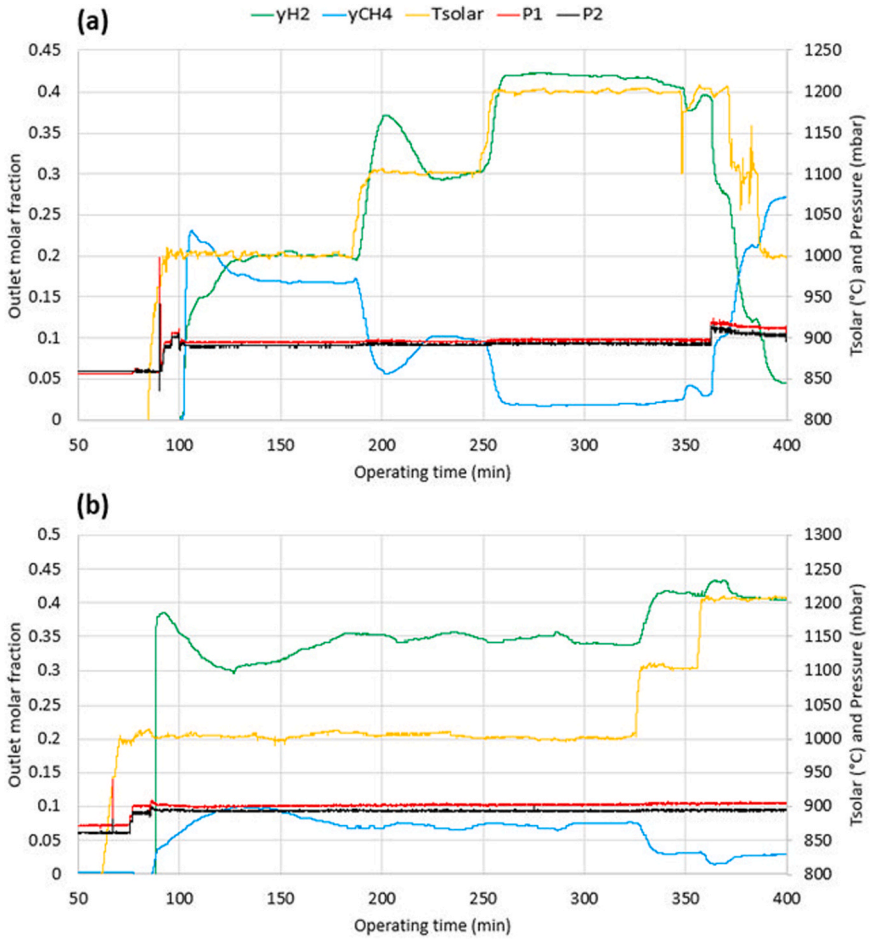

Fig. 3. Methane and hydrogen outlet mole fractions as well as temperature and pressure variations as a function of time in the long-run experiments with alumina bed: (a) Al_2O_3, (b) Ni-Al_2O_3.

Table 2
Results of methane cracking in beds of solid alumina particles without and with Ni catalyst ($Q_0 = 0.25$ NL/min and $y_{0,CH4} = 0.3$).

Medium	T (°C)	y_{H2}	y_{CH4}	y_{C2H2} (ppm)	y_{C2H4} (ppm)	y_{C2H6} (ppm)	X_{CH4} (%)	Y_{H2} (%)	Y_C (%)
Al_2O_3	1000	0.201	0.168	7	106	19	38	37	38
Al_2O_3	1100	0.301	0.098	19	200	22	62	58	62
Al_2O_3	1200	0.422	0.017	41	42	81	93	88	93
Ni-Al_2O_3	1000	0.355	0.068	95	0	0	73	72	72
Ni-Al_2O_3	1100	0.412	0.030	0	0	14	87	86	87
Ni-Al_2O_3	1200	0.431	0.014	0	0	0	94	91	94

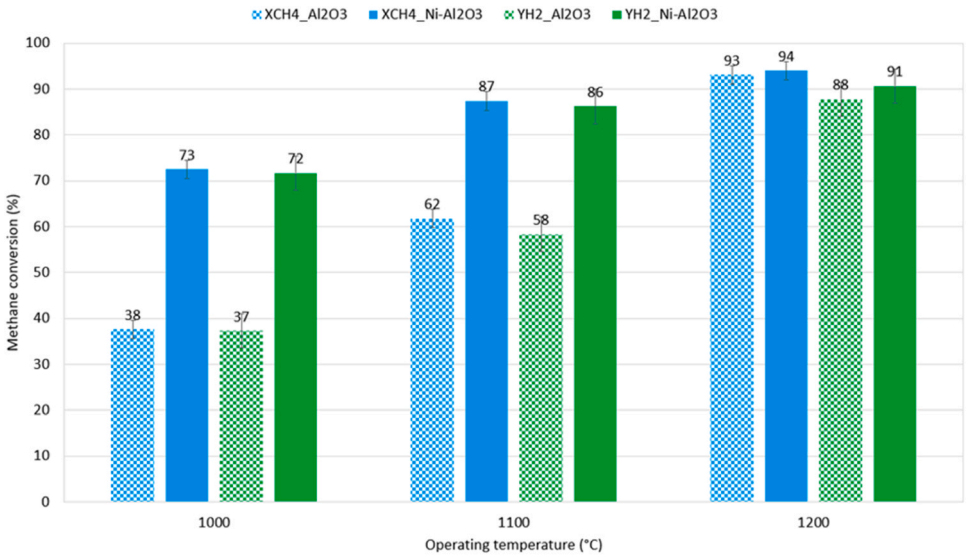

Fig. 4. Results of methane cracking in beds of solid alumina particles without and with Ni catalyst.

This first section investigated the effect of different media on methane cracking. Molten metals, including alloys, and molten salt (KCl) did not offer the desired catalytic activity to improve methane conversion. In contrast, when the melt was substituted by a bed of solid alumina particles, methane conversion was boosted, especially with the presence of Ni powder used as a catalyst. Indeed, the experiments with Ni metal catalyst in solid alumina particle bed were carried out to show that Ni catalyst in the solid form catalyzes the reaction in gas phase, whereas Ni particles dissolved in the molten metal bath were not shown to be active. This suggests that liquid phase catalysts are not efficient compared to solid phase catalysts. In addition, the solid particle bed was also studied for a comparison with the particle bed immersed in the liquid bath. In the next section, trials to optimize the process were focused on the injector in pure molten tin.

3.2. Effect of gas injectors and configurations

3.2.1. Quartz sparger

The experimental results with the quartz sparger are recapped in Table 3 along with those of Sn with open-end tube already presented in Table 1. The inlet flow rate was constant (0.25 NL/min) with methane inlet molar fraction of 0.3. Methane conversion at 1030 °C using the quartz sparger was still null (Fig. 5). When T was increased to 1130 °C, the conversion rose to only 18 % compared to 22 % using an ordinary injector. This difference was not meaningful given the 2.02 % relative uncertainty on methane conversion. Even in terms of hydrogen and carbon yield, results were close ($Y_{H2} = 13$ % vs. 12 % and $Y_C = 15$ % vs. 11 %, for the open-end injector and the sparger, respectively). Uncertainty bars shown in Fig. 5 confirm that all these differences were not high enough to deduce effects of the quartz injector. At 1230 °C, methane conversion reached 62 % using the sparger vs. 57 % using an open-end tube. The difference was still not significant whereas spargers should improve both hydrodynamics and heat and mass transfer.

The quartz sparger did not improve the performance compared to an ordinary open-end injector. To further understand the results, trials were performed with argon bubbling in water using the same quartz sparger (Figure S28). The injection in the first trial was the same as in the real methane cracking experiments (downward injection), while in the second the sparger was inserted from the bottom to inject upwards. The difference was clear in terms of bubbles size and distribution in the water. A downward injection led to coalescence below the pores of the sparger because the small bubbles at formation were trapped by the sparger itself. In upward injection, the bubbles were significantly smaller, and the flow was very similar to a bubbly regime with negligible

Table 3
Results of methane cracking in 100 mm-height bath of molten Sn ($Q_0 = 0.25$ NL/min and $y_{0,CH4} = 0.3$): open-end vs quartz sparger configuration.

Injector	T (°C)	y_{H2}	y_{CH4}	y_{C2H2} (ppm)	y_{C2H4} (ppm)	y_{C2H6} (ppm)	X_{CH4} (%)	Y_{H2} (%)	Y_C (%)
Open-end	1030	0.003	0.296	15	509	530	1	1	1
Open-end	1130	0.078	0.228	4840	5096	601	22	13	15
Open-end	1230	0.256	0.114	7142	2933	125	57	48	49
Quartz sparger	1030	0.001	0.299	8	953	787	0	0	0
Quartz sparger	1130	0.070	0.238	4051	5365	878	18	12	11
Quartz sparger	1230	0.301	0.097	8589	4256	363	62	60	51

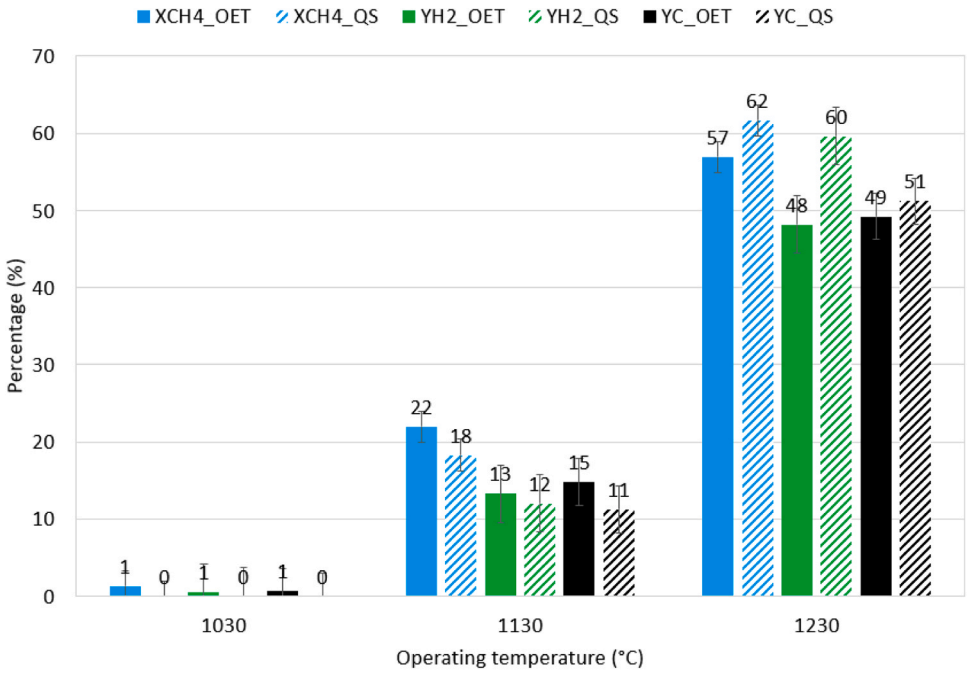

Fig. 5. Comparison of the results of methane cracking in a 100 mm tin bath (OET: open-end tube; QS: quartz sparger).

coalescence. In contrast, bubbles coalescence in downward injection made the flow very similar to that of an open-end tube, which decreased gas-liquid surface contact and limited bubbles residence time. Consequently, a sparger may be useless unless the pores are headed upwards. It should be noticed that implementation of up-flow spargers may introduce new issues linked to start up and shut down of the process. Continuous operation may be challenging as part of the molten metal may enter the sparger due to gravity and block the system due to metal solidification.

3.2.2. *PCW sparger vs. tungsten carbide (WC) bed*

The results of the set of experiments presented in Figure S3 are recapped in Table 4. The goal of these experiments was to compare the performance of the PCW sparger and the WC bed to a basic configuration with an open-end tube. It is worth to remind that PCW sparger leads to a sideway bubbling (lateral), unlike the quartz sparger with only downward bubbling.

Unlike previous experiments, pure methane was injected (no argon dilution) in the reactor while argon was directly fed at the reactor outlet for outlet gas dilution before gas analysis. The argon flow rate was chosen based on the inlet methane flow rate ($y_{0,CH4} = 0.3$). The lowest flow rate the flowmeter could feed was 0.05 NL/min. Thus, the fact that there was no argon fed in the reactor entrance allowed us to operate at low flow rates to avoid high pressures (due to high pressure loss of the spargers) in the injection tube that may lead to break it. For instance, in the experiment with WC bed, P1 increased to 982 mbar with P2 = 884 mbar even with methane inlet flow rate of 0.05 NL/min (ΔP = 98 mbar). Increasing methane inlet flow rate could have increased the pressure difference. Moreover, a low methane flow rate (0.05 NL/min) reduced the risk of coalescence and was closer to values reported in literature [6].

For each experiment, the goal was to achieve three runs at three different temperatures (1030–1130–1230 °C), for two different methane flow rates (0.05 and 0.1 NL/min). An intermediate flow rate of 0.075 NL/min was tested with the PCW sparger. As the height of the melt was higher than usual (150 mm currently), methane underwent partial decomposition in the inner tube, which was sometimes clogged before reaching the highest temperature (1230 °C). For instance, this was the case in the experiments with the open-end tube and the PCW sparger where the inner tube was clogged before reaching 1230 °C.

To simplify, the results with only 0.05 NL/min methane flow rate are represented in Fig. 6 for three different temperatures. Considering the uncertainty for X_{CH4}, the performance of the PCW sparger was not different compared to the basic open-end injector, neither at 1030 °C ($X_{CH4} = 0$ % vs. 2 %, respectively) nor at 1130 °C ($X_{CH4} = 31$ % vs. 33 %, respectively). The comparison at 1230 °C was not possible due to inner tube clogging. The low performance of the PCW sparger may be attributed to the non-uniform pores. The gas may have preferential

Table 4
Results of the set of experiments relevant to Figure S3 with OET (open-end tube); PCW-S (PCW sparger), and WC bed. Pure methane was injected through the melt in these experiments (with Ar dilution at the reactor outlet before gas analysis).

Experiment	$Q_{0,CH4}$ (NL/min)	$Q_{0,Ar}$ (NL/min)	T (°C)	y_{H2}	y_{CH4}	y_{C2H2} (ppm)	y_{C2H4} (ppm)	y_{C2H6} (ppm)	X_{CH4} (%)	Y_{H2} (%)	Y_C (%)
OET	0.05	0.12	1030	0.009	0.286	56	1109	534	2	2	1
OET	0.05	0.12	1130	0.170	0.180	2613	4671	447	33	32	27
OET	0.1	0.23	1130	0.097	0.230	3792	6381	645	20	17	13
PCW-S	0.05	0.12	1030	0.000	0.300	0	0	0	0	0	0
PCW-S	0.05	0.12	1130	0.151	0.188	3161	6207	624	31	28	23
PCW-S	0.075	0.175	1130	0.141	0.201	4106	6520	573	28	25	20
PCW-S	0.1	0.23	1130	0.126	0.213	4285	6690	525	24	22	16
WC bed	0.05	0.12	1030	0.069	0.238	22	2308	571	17	12	15
WC bed	0.05	0.12	1130	0.246	0.117	1759	5853	968	56	47	49
WC bed	0.05	0.12	1230	0.301	0.059	1388	3389	507	78	57	74

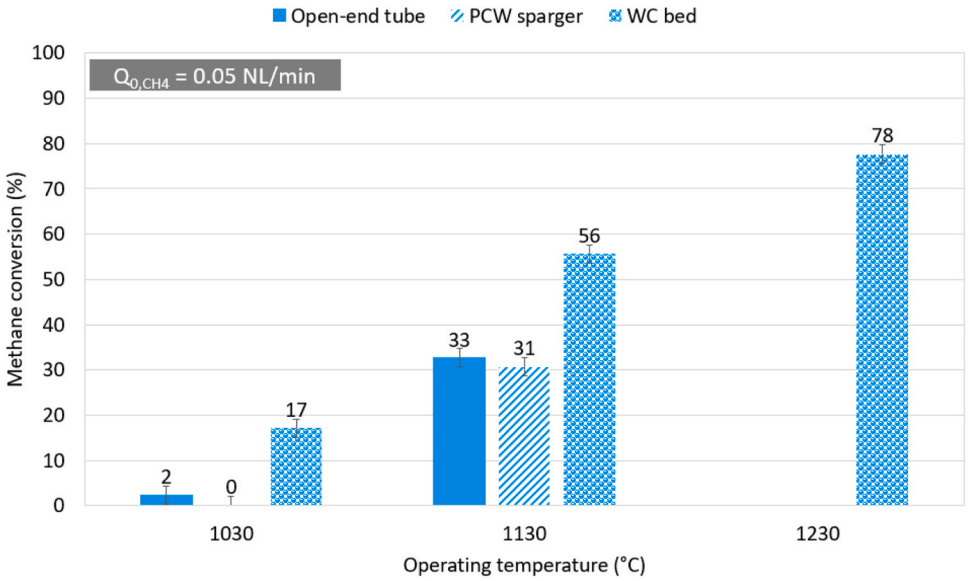

Fig. 6. Results of the experiments with the OET, homemade PCW sparger, and WC bed particles ($Q_{0,CH4}$ = 0.05 NL/min injected in the reactor).

paths through the largest pores, which limited the benefits of the sparger and resulted in the formation of large bubbles.

In contrast, the experiment with the WC bed significantly influenced the results with performance improvement due to an increased gas path length, while enabling efficient carbon separation on top of the melt (no carbon deposition on particles). Even at the lowest temperature (1030 °C), methane conversion was significant (17 %). This result was never observed in uncatalyzed gas-phase pyrolysis (negligible conversion at 1000 °C) [54]. The gap with the other two experiments was even larger at 1130 °C. At this temperature, X_{CH4} reached 56 % vs. only 33 % for the open-end tube and 31 % for the PCW sparger. During this experiment, the CH_4 conversion at 1230 °C was high (78 %). The fact that the WC bed improved the performance may be strongly related to the enhanced tortuosity (the gas path between the particles was enhanced). The WC particles were at least twice denser than molten tin, which helped them to settle down around the orifice of the inner tube. Thus, methane gas coming out from the orifice had a large contact surface with the bed. Additionally, the bed may have behaved as a porous zone leading to the generation of smaller bubbles with a longer path flow between particles, thus increasing the residence time of bubbles. Methane conversion was thus enhanced, while carbon recovery at the melt surface was advantageously possible. Other options to increase efficiently the residence time may be a gas sparger headed upwards (to decrease the size of bubbles and their rising velocity) or an increase of the molten bath height [52].

4. Conclusions

Several strategies including medium type and gas injection configuration were proposed and tested to improve solar methane pyrolysis in a bubble column reactor.

(i) Different molten media (Sn, $Ni_{0.18}Sn_{0.82}$, $Cu_{0.45}Bi_{0.55}$, and KCl) were tested for the aim of an enhanced methane conversion. The experiments were carried out at a fixed gas flow rate (0.25 NL/min) and CH_4 inlet molar fraction (0.3). At 1030 °C and 1130 °C, none of these melts increased CH_4 conversion compared to a pure Sn melt, which suggests that catalytic effects in liquid-phase (NiSn, CuBi alloys) were not effective. Only at 1230 °C, using KCl resulted in X_{CH4} = 72 % compared to 57 % for pyrolysis in pure Sn. The improved conversion only at the highest temperature for KCl was attributed to carbon dispersion in the salt, which may have changed the physical properties of the bulk, resulting in enhanced bubbles hydrodynamics and residence time.

Carbon formed in metallic alloys was generally graphitic with a sheet-like structure, especially in NiSn, and was contaminated with metals. However, some large spheres were easily observed in the carbon sample from $Cu_{0.45}Bi_{0.55}$ experiment. These spheres were identified as Bi contamination. The carbon formed in KCl was still graphitic, however, it was in the form of dispersed spheres. The absence of sheet-like structure in carbon from KCl experiment was caused by the dispersion of carbon in the salt due to an inefficient separation related to relatively close densities of carbon and KCl, compared to carbon and metals.

Substituting the melt by a bed of solid alumina particles resulted in a drastic increase in methane conversion (X_{CH4} = 38 %) at only 1000 °C. Adding nickel powder catalyst to the bed boosted conversion further to 73 % at the same temperature (1000 °C). These experiments proved that a solid particle bed boosts heat transfer and reaction active surface, and hence methane conversion. In addition, molten alloys (NiSn, CuBi) did not act as effective liquid-phase catalysts for methane pyrolysis unlike solid state catalyst (Ni/Al_2O_3).

(ii) Another way of process enhancement was the injection design. A quartz sparger was used to inject methane in a pure molten tin reactor. The result was not significantly different from that with a normal open-end injector (X_{CH4} = 62 % vs. 57 % at 1230 °C for the sparger and the open-end tube, respectively). The low performance of the sparger was related to the downward direction of injection. It might have resulted in smaller bubbles generation, however, they were trapped under the pores and thus coalesced. An upward injection direction should be more favorable to benefit from the sparger through smaller bubbles generation and a bubbly flow.

A customized sparger (PCW sparger) made from a tube cemented in a porous material was also investigated in a 150 mm tin bath. This sparger did not enhance conversion compared to an open-end tube (X_{CH4} = 31 % vs. 33 % for the PCW sparger and the open-end tube, respectively). In contrast, when a solid bed of WC particles (100 mm height) was immersed in molten tin (total height of tin + particles: 150 mm), methane conversion was significantly improved (X_{CH4} = 17 % vs. 2 % at 1030 °C and 56 % vs. 33 % at 1130 °C, for the experiment with WC bed around the orifice and that with an open-end injector, respectively). WC was much denser than Sn, thus the particles settled down around the orifice and behaved as a porous zone, which increased the residence time of bubbles.

Future work should focus on detailed characterization of catalysis in molten media and associated reaction mechanisms. In order to draw fair

conclusions about the catalytic activity of liquid media, it is also advised to always provide results compared with molten tin as reference in the same reactor configuration and operating conditions to avoid biased interpretation of the methane pyrolysis performance.

CRediT authorship contribution statement

Sylvain Rodat: Writing – review & editing, Visualization, Validation, Supervision, Resources, Project administration, Methodology, Investigation, Funding acquisition, Formal analysis, Data curation, Conceptualization. **Malek Msheik:** Writing – original draft, Visualization, Validation, Software, Methodology, Investigation, Formal analysis, Data curation. **Stéphane Abanades:** Writing – review & editing, Visualization, Validation, Supervision, Software, Resources, Project administration, Methodology, Investigation, Funding acquisition, Formal analysis, Data curation, Conceptualization.

Declaration of Competing Interest

The authors declare that they have no known competing financial interests or personal relationships that could have appeared to influence the work reported in this paper.

Data Availability

Data will be made available on request.

Acknowledgments

The authors thank R. Garcia for his support in the design and installation of the solar reactor, R. Rodriguez and E. Guillot for their support to set the data acquisition system, and E. Bêche for XRD analysis. The authors are also grateful to N. Boullet for machining proper samples for characterization. Aforementioned persons are all part of PROMES-CNRS laboratory. This work was partially supported by the French "Investments for the future" program managed by the National Agency for Research.

Appendix A. Supporting information

Supplementary data associated with this article can be found in the online version at doi:10.1016/j.jaap.2024.106756.

References

[1] International Energy Agency n.d. ⟨https://www.iea.org/reports/global-hydrogen-review-2022/executive-summary⟩ (Accessed August 20, 2023).
[2] V. Tacchino, P. Costamagna, S. Rosellini, V. Mantelli, A. Servida, Multi-scale model of a top-fired steam methane reforming reactor and validation with industrial experimental data, Chem. Eng. J. 428 (2022) 131492, https://doi.org/10.1016/j.cej.2021.131492.
[3] Q. Zhang, S. Shan, J. Yu, Z. Zhou, K.H. Luo, Coal gasification process driven by concentrated solar radiation for carbon neutralization: reaction and energy characteristics, Chem. Eng. J. 450 (2022) 138286, https://doi.org/10.1016/j.cej.2022.138286.
[4] T. Terlouw, C. Bauer, R. McKenna, M. Mazzotti, Large-scale hydrogen production via water electrolysis: a techno-economic and environmental assessment, Energy Environ. Sci. 15 (2022) 3583–3602, https://doi.org/10.1039/D2EE01023B.
[5] M. Keller, A. Matsumura, A. Sharma, Spray-dried Fe/Al2O3 as a carbon carrier for COx-free hydrogen production via methane cracking in a fluidized bed process, Chem. Eng. J. 398 (2020) 125612, https://doi.org/10.1016/j.cej.2020.125612.
[6] M. Msheik, S. Rodat, S. Abanades, Methane cracking for hydrogen production: a review of catalytic and molten media pyrolysis, Energies 14 (2021) 3107, https://doi.org/10.3390/en14113107.
[7] A.M. Amin, E. Croiset, W. Epling, Review of methane catalytic cracking for hydrogen production, Int J. Hydrog. Energy 36 (2011) 2904–2935, https://doi.org/10.1016/j.ijhydene.2010.11.035.
[8] Z. Wan, S. Yang, G. Bao, J. Hu, H. Wang, Multiphase particle-in-cell simulation study of sorption enhanced steam methane reforming process in a bubbling fluidized bed reactor, Chem. Eng. J. 429 (2022) 132461, https://doi.org/10.1016/j.cej.2021.132461.
[9] S. Rodat, S. Abanades, G. Flamant, High-temperature solar methane dissociation in a multitubular cavity-type reactor in the temperature range 1823−2073 K, Energy Fuels 23 (2009) 2666–2674, https://doi.org/10.1021/ef900037v.
[10] S. Abanades, H. Kimura, H. Otsuka, Kinetic investigation of carbon-catalyzed methane decomposition in a thermogravimetric solar reactor, Int J. Hydrog. Energy 40 (2015) 10744–10755, https://doi.org/10.1016/j.ijhydene.2015.07.023.
[11] S. Rodat, S. Abanades, E. Grivei, G. Patrianakos, A. Zygogianni, A. G. Konstandopoulos, et al., Characterisation of carbon blacks produced by solar thermal dissociation of methane, Carbon N. Y 49 (2011) 3084–3091, https://doi.org/10.1016/j.carbon.2011.03.030.
[12] S. Abanades, H. Kimura, H. Otsuka, A drop-tube particle-entrained flow solar reactor applied to thermal methane splitting for hydrogen production, Fuel 153 (2015) 56–66, https://doi.org/10.1016/j.fuel.2015.02.103.
[13] F.M. Berndt, O.W. Perez-Lopez, Catalytic decomposition of methane over Ni/SiO2: influence of Cu addition, React. Kinet. Mech. Catal. 120 (2017) 181–193, https://doi.org/10.1007/s11144-016-1096-4.
[14] N. Bayat, M. Rezaei, F. Meshkani, Methane decomposition over Ni-Fe/Al2O3 catalysts for production of COx-free hydrogen and carbon nanofiber, Int. J. Hydrog. Energy 41 (2016) 1574–1584, https://doi.org/10.1016/j.ijhydene.2015.10.053.
[15] S. Patel, S. Kundu, P. Halder, M.H. Marzbali, K. Chiang, A. Surapaneni, et al., Production of hydrogen by catalytic methane decomposition using biochar and activated char produced from biosolids pyrolysis, Int. J. Hydrog. Energy 45 (2020) 29978–29992, https://doi.org/10.1016/j.ijhydene.2020.08.036.
[16] M. Msheik, S. Rodat, S. Abanades, CFD simulation of a hybrid solar/electric reactor for hydrogen and carbon production from methane cracking, Fluids 8 (2023) 18, https://doi.org/10.3390/fluids8010018.
[17] C. Tanggarnjanavalukul, W. Donphai, T. Witoon, M. Chareonpanich, J. Limtrakul, Deactivation of nickel catalysts in methane cracking reaction: effect of bimodal meso–macropore structure of silica support, Chem. Eng. J. 262 (2015) 364–371, https://doi.org/10.1016/j.cej.2014.09.112.
[18] Tyrer D. Production of hydrogen U.S. Patent 1 803 221, Apr. 28,. The United States Patent Office. 1803221, 1931. https://doi.org/10.1126/science.53.1377.481.
[19] L.J.J. Catalan, B. Roberts, E. Rezaei, A low carbon methanol process using natural gas pyrolysis in a catalytic molten metal bubble reactor, Chem. Eng. J. 462 (2023) 142230, https://doi.org/10.1016/j.cej.2023.142230.
[20] V.E. Parfenov, N.V. Nikitchenko, A.A. Pimenov, A.E. Kuz'min, M.V. Kulikova, O. B. Chupichev, et al., Methane pyrolysis for hydrogen production: specific features of using molten metals, Russ. J. Appl. Chem. 93 (2020) 625–632, https://doi.org/10.1134/S1070427220050018.
[21] S.R. Patlolla, K. Katsu, A. Sharafian, K. Wei, O.E. Herrera, W. Mérida, A review of methane pyrolysis technologies for hydrogen production, Renew. Sustain Energy Rev. 181 (2023) 113323, https://doi.org/10.1016/j.rser.2023.113323.
[22] M. McConnachie, M. Konarova, S. Smart, Literature review of the catalytic pyrolysis of methane for hydrogen and carbon production, Int. J. Hydrog. Energy 48 (2023) 25660–25682, https://doi.org/10.1016/j.ijhydene.2023.03.123.
[23] D.C. Upham, V. Agarwal, A. Khechfe, Z.R. Snodgrass, M.J. Gordon, H. Metiu, et al., Catalytic molten metals for the direct conversion of methane to hydrogen and separable carbon, Science 358 (2017) 917–921, https://doi.org/10.1126/science.aao5023.
[24] C. Palmer, M. Tarazkar, H.H. Kristoffersen, J. Gelinas, M.J. Gordon, E. W. McFarland, et al., Methane pyrolysis with a molten Cu-Bi alloy catalyst, ACS Catal. 9 (2019) 8337–8345, https://doi.org/10.1021/acscatal.9b01833.
[25] K. Wang, W.S. Li, X.P. Zhou, Hydrogen generation by direct decomposition of hydrocarbons over molten magnesium, J. Mol. Catal. A Chem. 283 (2008) 153–157, https://doi.org/10.1016/j.molcata.2007.12.018.
[26] J. Zeng, M. Tarazkar, T. Pennebaker, M.J. Gordon, H. Metiu, E.W. McFarland, Catalytic methane pyrolysis with liquid and vapor phase tellurium, ACS Catal. 10 (2020) 8223–8230, https://doi.org/10.1021/acscatal.0c00805.
[27] N. Zaghloul, S. Kodama, H. Sekiguchi, Hydrogen production by methane pyrolysis in a molten-metal bubble column, Chem. Eng. Technol. 44 (2021) 1986–1993, https://doi.org/10.1002/ceat.202100210.
[28] M. Plevan, T. Geißler, A. Abánades, K. Mehravaran, R.K. Rathnam, C. Rubbia, et al., Thermal cracking of methane in a liquid metal bubble column reactor: experiments and kinetic analysis, Int J. Hydrog. Energy 40 (2015) 8020–8033, https://doi.org/10.1016/j.ijhydene.2015.04.062.
[29] M. Serban, M.A. Lewis, C.L. Marshall, R.D. Doctor, Hydrogen production by direct contact pyrolysis of natural gas, Energy Fuels 17 (2003) 705–713, https://doi.org/10.1021/ef020271q.
[30] T. Geißler, M. Plevan, A. Abánades, A. Heinzel, K. Mehravaran, R.K. Rathnam, et al., Experimental investigation and thermo-chemical modeling of methane pyrolysis in a liquid metal bubble column reactor with a packed bed, Int J. Hydrog. Energy 40 (2015) 14134–14146, https://doi.org/10.1016/j.ijhydene.2015.08.102.
[31] E. Busillo, B. de Caprariis, M.P. Bracciale, V. Cosentino, M. Damizia, G. Iaquaniello, et al., Methane cracking in molten tin for hydrogen and carbon production—a comparison with homogeneous gas phase process, Front Chem. Sci. Eng. 18 (2024) 82, https://doi.org/10.1007/s11705-024-2437-x.
[32] D. Scheiblehner, D. Neuschitzer, S. Wibner, A. Sprung, H. Antrekowitsch, Hydrogen production by methane pyrolysis in molten binary copper alloys, Int J. Hydrog. Energy 48 (2023) 6233–6243, https://doi.org/10.1016/j.ijhydene.2022.08.115.
[33] S. Sorcar, B.A. Rosen, Methane pyrolysis using a multiphase molten metal reactor, ACS Catal. 13 (2023) 10161–10166, https://doi.org/10.1021/acscatal.3c02955.
[34] B. Parkinson, C.F. Patzschke, D. Nikolis, S. Raman, D.C. Dankworth, K. Hellgardt, Methane pyrolysis in monovalent alkali halide salts: Kinetics and pyrolytic carbon properties, Int J. Hydrog. Energy 46 (2021) 6225–6238, https://doi.org/10.1016/j.ijhydene.2020.11.150.

[35] B. Parkinson, C.F. Patzschke, D. Nikolis, S. Raman, K. Hellgardt, Molten salt bubble columns for low-carbon hydrogen from CH4 pyrolysis: mass transfer and carbon formation mechanisms, Chem. Eng. J. 417 (2021) 127407, https://doi.org/10.1016/j.cej.2020.127407.
[36] D. Kang, N. Rahimi, M.J. Gordon, H. Metiu, E.W. McFarland, Catalytic methane pyrolysis in molten MnCl2-KCl, Appl. Catal. B Environ. 254 (2019) 659–666, https://doi.org/10.1016/j.apcatb.2019.05.026.
[37] D. Bae, Y. Kim, E.H. Ko, S. Ju Han, J.W. Lee, M. Kim, et al., Methane pyrolysis and carbon formation mechanisms in molten manganese chloride mixtures, Appl. Energy 336 (2023) 120810, https://doi.org/10.1016/j.apenergy.2023.120810.
[38] A. Sheil, M. Konarova, M. McConnachie, S. Smart, Selectivity and reaction kinetics of methane pyrolysis to produce hydrogen in catalytically active molten salts, Appl. Energy 364 (2024) 123137, https://doi.org/10.1016/j.apenergy.2024.123137.
[39] M. McConnachie, A. Sheil, M. Konarova, S. Smart, Evaluation of heterogeneous metal-sulfide molten salt slurry systems for hydrogen production through methane pyrolysis, Int J. Hydrog. Energy 49 (2024) 981–991, https://doi.org/10.1016/j.ijhydene.2023.08.072.
[40] N. Rahimi, D. Kang, J. Gelinas, A. Menon, M.J. Gordon, H. Metiu, et al., Solid carbon production and recovery from high temperature methane pyrolysis in bubble columns containing molten metals and molten salts, Carbon N. Y. 151 (2019) 181–191, https://doi.org/10.1016/j.carbon.2019.05.041.
[41] B.J. Leal Pérez, J.A. Medrano Jiménez, R. Bhardwaj, E. Goetheer, M. van Sint Annaland, F. Gallucci, Methane pyrolysis in a molten gallium bubble column reactor for sustainable hydrogen production: Proof of concept & techno-economic assessment, Int J. Hydrog. Energy 46 (2021) 4917–4935, https://doi.org/10.1016/j.ijhydene.2020.11.079.
[42] J. Kim, C. Oh, H. Oh, Y. Lee, H. Seo, Y.K. Kim, Catalytic methane pyrolysis for simultaneous production of hydrogen and graphitic carbon using a ceramic sparger in a molten NiSn alloy, Carbon N. Y. 207 (2023) 1–12, https://doi.org/10.1016/j.carbon.2023.02.053.
[43] G.A. Von Wald, M.S. Masnadi, D.C. Upham, A.R. Brandt, Optimization-based technoeconomic analysis of molten-media methane pyrolysis for reducing industrial sector CO 2 emissions, Sustain Energy Fuels 4 (2020) 4598–4613, https://doi.org/10.1039/D0SE00427H.
[44] I.V. Kudinov, A.A. Pimenov, Y.A. Kryukov, G.V. Mikheeva, A theoretical and experimental study on hydrodynamics, heat exchange and diffusion during methane pyrolysis in a layer of molten tin, Int J. Hydrog. Energy 46 (2021) 10183–10190, https://doi.org/10.1016/j.ijhydene.2020.12.138.
[45] A.A. Munera Parra, D.W. Agar, Molten metal capillary reactor for the high-temperature pyrolysis of methane, Int J. Hydrog. Energy 42 (2017) 13641–13648, https://doi.org/10.1016/j.ijhydene.2016.12.044.
[46] M.R. Abdollahi, G.J. Nathan, M. Jafarian, Process configurations to lower the temperature of methane pyrolysis in a molten metal bath for hydrogen production, Int. J. Hydrog. Energy 48 (2023) 39805–39822, https://doi.org/10.1016/j.ijhydene.2023.08.186.
[47] B. de Caprariis, M. Damizia, E. Busillo, P. De Filippis, Advances in molten media technologies for methane pyrolysis, Adv. Chem. Eng. 61 (2023) 319–356, https://doi.org/10.1016/bs.ache.2023.03.001.
[48] N.A. Kazakis, I.D. Papadopoulos, A.A. Mouza, Bubble columns with fine pore sparger operating in the pseudo-homogeneous regime: gas hold up prediction and a criterion for the transition to the heterogeneous regime, Chem. Eng. Sci. 62 (2007) 3092–3103, https://doi.org/10.1016/j.ces.2007.03.004.
[49] I.V. Kudinov, Y.V. Velikanova, M.V. Nenashev, T.F. Amirov, A.A. Pimenov, Methane pyrolysis in molten media for hydrogen production: a review of current advances, Pet. Chem. 63 (2023) 1017–1026, https://doi.org/10.1134/S0965544123080078.
[50] T.I. Korányi, M. Németh, A. Beck, A. Horváth, Recent advances in methane pyrolysis: turquoise hydrogen with solid carbon production, Energies 15 (2022) 6342, https://doi.org/10.3390/en15176342.
[51] S. Cheon, M. Byun, D. Lim, H. Lee, H. Lim, Parametric study for thermal and catalytic methane pyrolysis for hydrogen production: techno-economic and scenario analysis, Energies 14 (2021) 6102, https://doi.org/10.3390/en14196102.
[52] J. Boo, E.H. Ko, N.-K. Park, C. Ryu, Y.-H. Kim, J. Park, et al., Methane pyrolysis in molten potassium chloride: an experimental and economic analysis, Energies 14 (2021) 8182, https://doi.org/10.3390/en14238182.
[53] S. Rodat, S. Abanades, G. Flamant, Methane decarbonization in indirect heating solar reactors of 20 and 50 kW for a CO2-free production of hydrogen and carbon black, J. Sol. Energy Eng. 133 (2011) 031001, https://doi.org/10.1115/1.4004238.
[54] M. Msheik, S. Rodat, S. Abanades, Experimental comparison of solar methane pyrolysis in gas-phase and molten-tin bubbling tubular reactors, Energy 260 (2022) 124943, https://doi.org/10.1016/j.energy.2022.124943.
[55] M. Msheik, S. Rodat, S. Abanades, Enhancing molten tin methane pyrolysis performance for hydrogen and carbon production in a hybrid solar/electric bubbling reactor, Int J. Hydrog. Energy 49 (2024) 962–980, https://doi.org/10.1016/j.ijhydene.2023.08.068.
[56] H.B. Palmer, T.J. Hirt, The activation energy for the pyrolysis of methane, J. Phys. Chem. 67 (1963) 709–711, https://doi.org/10.1021/j100797a502.
[57] P. Nash, A. Nash, The Ni−Sn (Nickel-Tin) system, Bull. Alloy Ph. Diagr. 6 (1985) 350–359, https://doi.org/10.1007/BF02880521.
[58] A. Iveković, N. Omidvari, B. Vrancken, K. Lietaert, L. Thijs, K. Vanmeensel, et al., Selective laser melting of tungsten and tungsten alloys, Int. J. Refract Met. Hard Mater. 72 (2018) 27–32, https://doi.org/10.1016/j.ijrmhm.2017.12.005.
[59] N. Kawano, Y. Tamai, M. Kondo, Excellent corrosion resistance of tungsten materials in liquid tin, 1205068–1205068, Plasma Fusion Res 15 (2020), https://doi.org/10.1585/pfr.15.1205068.
[60] B.B. Alchagirov, A.M. Chochaeva, Temperature dependence of the density of liquid tin, High. Temp. 38 (2000) 44–48, https://doi.org/10.1007/BF02755565.
[61] A.D.D. Kirshenbaum, J.A.A. Cahill, P.J.J. McGonigal, A.V.V. Grosse, The density of liquid NaCl and KCl and an estimate of their critical constants together with those of the other alkali halides, J. Inorg. Nucl. Chem. 24 (1962) 1287–1296, https://doi.org/10.1016/0022-1902(62)80205-X.